Journal of Alloys and Compounds 893 (2022) 162060

Contents lists available at ScienceDirect

Journal of Alloys and Compounds

journal homepage: www.elsevier.com/locate/jalcom

Structure and phase transformations in gas atomized AlCoCrFeNi high entropy alloy powders

Dennis Karlsson[a,*], Premysl Beran[b,c], Lars Riekehr[a], Jo-Chi Tseng[d], Peter Harlin[e], Ulf Jansson[a], Johan Cedervall[f]

[a] Department of Chemistry - Ångström Laboratory, Uppsala University, Box 538, SE-751 21 Uppsala, Sweden
[b] Nuclear Physics Institute, Academy of Sciences of the Czech Republic, 25068 Rez, Czech Republic
[c] European Spallation Source ESS ERIC, Box 176, SE-221 00 Lund, Sweden
[d] Deutsches Elektronen Synchrotron DESY, Notkestrasse 85, D-22603 Hamburg, Germany
[e] Sandvik Additive Manufacturing, Sandvik AB, Box 510, SE-101 30 Stockholm, Sweden
[f] Department of Materials and Environmental Chemistry, Stockholm University, Svante Arrhenius väg 16C, SE-106 91 Stockholm, Sweden

ARTICLE INFO

Article history:
Received 29 June 2021
Received in revised form 13 September 2021
Accepted 19 September 2021
Available online 30 September 2021

Keywords:
High-entropy alloy
HEA
Diffraction
X-ray scattering
Neutron scattering
Additive manufacturing

ABSTRACT

In this study, the crystal structure and phase stability of gas atomized equiatomic AlCoCrFeNi powder was investigated. This alloy is usually described as a high entropy alloy forming a solid solution phase stabilized by a high mixing entropy. However, thermodynamic calculations show that the high entropy phase is stable only at very high temperatures close to the melting point and that a mixture of several phases are the most stable state at lower temperatures. This suggest that kinetic effects may influence the phase composition of atomized powder. The unique features of X-ray diffraction, neutron diffraction as well as transmission electron microscopy were used to study the atomic structure of the atomized powder in detail. The results show that the powder crystallises in an ordered B2 (CsCl-type) structure with a preferred site occupation of Al and Fe on the (½ ½ ½) position and Co and Ni on the (0 0 0) position. During heat-treatment of the powder, the B2 phase decomposes into fcc and σ phases and the final phase composition is highly dependent on the heating rate. The effect of heat-treatment on the atomized powder was also investigated and revealed a significant phase transformation with e.g. the formation of σ phase preferably at the surface of the powder particles. The phase content was also dependent on the size fraction of the powder particles. Sintering of green bodies made with different heat cycles showed that the phase composition of the starting material had a significant impact on the final phase composition and microstructure of the sintered components. The results illustrate the importance of well-defined powder materials for powder consolidation, especially additive manufacturing (binder jetting) of high entropy alloys.

1. Introduction

The development of high-entropy alloys (HEA) has grown rapidly since their discovery by Cantor et al. [1] and Yeh et al. [2] in 2004. In HEAs, solid solutions with simple crystal structures, e.g. body centred cubic (bcc), cubic close packing (ccp, also known as face centred cubic, fcc) or hexagonal close packing (hcp), are assumed to form due to the high configurational entropy from the mixture of at least five elements in near equiatomic concentrations. Many of these alloys possess desirable properties such as high strength at various temperatures, high hardness, high ductility, and excellent wear resistance [3–8]. Additionally, promising oxidation resistance, corrosion resistance and hydrogen storage capabilities have been displayed by several HEAs [9–13]. As the influence of entropy on the formation of these alloys is unclear, the terms multi-principal element alloys (MPEAs) or complex, concentrated alloys (CCAs) have been widely accepted as alternative descriptions. An excellent review of HEAs can be found in a paper by Miracle and Senkov [14].

Many so-called high entropy alloys are not stable solid solutions, and thermodynamic calculations show that they form a phase mixture at equilibrium in a wide temperature range [15]. The fact that they experimentally form solid solutions can be explained by kinetic factors where a fast cooling rate from the melt or high temperatures limits the diffusion rate of the elements, leaving a metastable solid solution. One example of this is found for the AlCoCrFeNi alloy, where solid solution phase (HEA) is stable only at

* Corresponding author.
E-mail address: dennis.karlsson@kemi.uu.se (D. Karlsson).

https://doi.org/10.1016/j.jallcom.2021.162060
0925-8388/

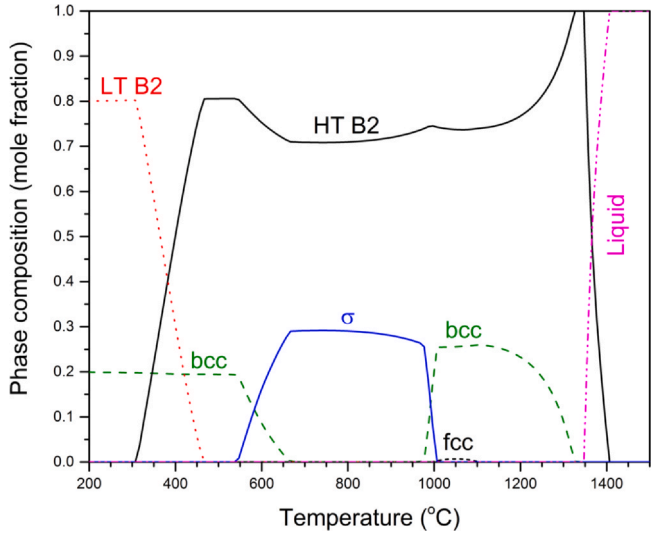

Fig. 1. Phase diagram of AlCoCrFeNi calculated by the CALPHAD method. The results have been adapted from ref. [15], but is reproduced here to facilitate the discussion.

high temperatures close to the melting point, while a mixture of B2, bcc, σ and minor amounts of fcc are thermodynamically stable at lower temperatures (see Fig. 1). Extended annealing experiments of the alloy at selected temperatures, followed by rapid quenching of the HEA, shows a phase composition in agreement with the thermodynamic calculations [15]. Experimental studies, however, of alloys formed from a melt and more slowly cooled down to room temperature typically show a B2/bcc phase mixture, supporting the importance of slow kinetics during the solidification process [10,15–20]. Furthermore, it has been shown that a single-phase HEA can be obtained in e.g., the AlCoCrFeNi, AlCoCrFeNiMn and MgAlSiCrFeNi systems by mechanical alloying [21–23]. Upon annealing, however, the single-phase configuration is not stable and different intermetallic phases may form, further suggesting that the HEA is only stable at high temperatures.

The good oxidation resistance and promising mechanical properties make the AlCoCrFeNi alloy one of the most studied HEAs, and a candidate for high-temperature applications. Most studies produce AlCoCrFeNi by arc melting or casting, but recently the use of additive manufacturing has been explored to produce high strength components [15,20,24,25]. Fujieda et al. [24] showed an increase of the yield strength and fracture strength of up to 60% of a selective electron beam melted (SEBM) produced sample compared to the cast alternative. Furthermore, the production of components with intriguing microstructures by annealing of binder jetting produced parts was shown to enhance both yield and fracture strength [15]. When comparing the phase composition and microstructure in different studies, it is clear that the choice of manufacturing process used is very important and that differences in kinetics have a strong effect on the final product.

In additive manufacturing (using a powder bed fusion technique) as well as other powder consolidation processes, a fully alloyed metal powder of the alloy can be used as feedstock material. The powder is usually manufactured by conventional metallurgy followed by atomization. In the atomization step, a steam of molten metal is disintegrated into droplets of molten metal by a high pressure gas and the droplets solidifies into a powder [26]. The powder is then sieved into size fractions to be utilized as feedstock in different powder consolidating processes. Based on the results in Fig. 1, it is expected that the microstructure and phase composition of the AlCoCrFeNi powder (as well as many other HEAs) are strongly dependent on kinetic effects during the atomization process. Hence, the cooling rate in the manufacturing process will be of great importance for the phase formation and the microstructure of the high-entropy alloy. In the gas-atomization process the cooling rate is estimated to be around 10^4-10^6 K/s depending on the particle size [26–28], allowing formation of phases far from equilibrium. This effect may be of importance when utilizing non-melting powder consolidating processes such as solid state sintering included in the binder jetting technique [15] as the last densification step. It has previously been shown that components of AlCoCrFeNi can successfully be produced by binder jetting [15]. However, the as-built components exhibit a brittle behaviour due to the presence of brittle phases such as the σ phase, and heat-treatments are therefore required to obtain a functional material. The phase composition and microstructure of the feedstock powder potentially influences the manufactured components and may be utilized to tune the final properties. Additionally, different powder size distributions will exhibit different sintering behaviour and could result in different phase compositions and microstructures of the final component.

The aim of this study is to increase the understanding of the microstructure and phase formation of gas atomized AlCoCrFeNi with different particle sizes. Furthermore, the σ phase is detrimental for the properties of the AlCoCrFeNi alloy and it is therefore of great interest with a methodology to avoid formation of brittle phases. Hence, the effect of pre-annealing of the powder on the final microstructure was investigated. A combination of X-ray and neutron diffraction with electron microscopy was utilized to determine the crystal structure, with emphasis on the atomic occupations in the as-atomized powder state.

2. Experimental procedure

Powder of the AlCoCrFeNi HEA was pre-alloyed and gas atomized by Sandvik Osprey™ and sized into several different powder particle size distributions (PSD). In this study, the PSD 10–45 µm and < 32 µm were investigated, PSDs that are commonly used for laser powder bed fusion and binder jetting, respectively. SEM images of the powders can be found in supplementary information (SI), Fig. S1. All sintered components were prepared from powder with PSD < 32 µm. Two different powder conditions were evaluated, as-atomized powder condition and pre-annealed powder condition. The as-atomized powder condition is as obtained directly after sizing into desired PSD, while in the pre-annealed condition the powder was heat-treated at 800 °C for 1 h after sizing. Sintering experiments on the different powder conditions were performed at 1320 °C for 4 h followed by furnace cooling, the atmosphere was kept inert by flowing Ar (g) of 50 ml/min after flushing for 30 min. Prior to sintering, the powder was mixed with 2 wt% binder (consisting of 5 wt% polyvinyl alcohol in water) and pressed into a pellet. The binder was dried in a furnace at 150 °C for 2 h to remove the water. The binder was removed by a pre-sintering step at 435–650 °C.

The loose powders were analysed with *ex-* and in-situ diffraction utilizing several radiation sources. *In-situ* X-ray diffraction (XRD) was performed at the P02.1 beamline at the synchrotron DESY (Hamburg, Germany). The wavelength was determined to 0.206578 Å using a LaB_6 standard. A PerkinElmer XRD1621 detector and an exposure time of 5 s per diffraction pattern were used during the experiments. The samples were mounted in a sapphire tube and mounted in a sample cell described by Höglin et al. [29]. The diffraction patterns were collected during continuous heating of the sample to 900 °C with a heating rate of 10 °C/min and aged for 10 min before turning the heating off and letting the sample rapidly cool down to room temperature. The neutron powder diffraction (NPD) experiments were performed on the D1B and MEREDIT instruments at ILL (Grenoble, France) and the Nuclear Physics Institute (Rez, Czech Republic), respectively. The diffraction patterns were recorded at discrete temperatures upon heating from room temperature (RT) to 800 °C. At D1B a Ge monochromator (reflection 311)

was used, giving a wavelength of 1.28 Å, while a mosaic Cu crystal (reflection 220) and a bent Si single crystal (reflection 442) giving wavelengths of 1.46 Å and 1.27 Å were used at MEREDIT. Additionally, *ex-situ* XRD was performed on the sintered samples using a Bruker D8 Advance diffractometer operating with CuKα radiation and equipped with a Lynx-eye XE position sensitive detector.

Refinements of all diffraction data were performed using the Rietveld method [30] implemented in the FullProf software [31]. A Thompson-Cox-Hastings pseudo-Voigt profile function was used to describe the diffraction peaks and the background was described from interpolation from chosen and refinable points. In the refinements, the zero point, background, scale factor, peak shape, half-width parameters, unit cell parameters, atomic occupancies, isotropic temperature parameter and atomic coordinates were varied. The in-situ 2D XRD patterns were first reduced with the software Fit2D [32] to acquire 1D patterns. The reduced diffraction patterns were refined in a sequential mode in FullProf and all parameters were fixed, except for the scale factors, correlated to the amount of the phases. To gain maximum information of the atomic positions and occupancies, joined refinements were performed for the in-house and the two neutron diffraction data sets at room temperature.

The TEM analyses were carried out in TEM and STEM mode using a probe corrected FEI Titan Themis instrument operated at 200 kV acceleration voltage equipped with the SuperX EDS system. For nanobeam diffraction (NBD), the TEM was operated in μProbe STEM mode with a probe size of approximately 5 nm to record diffraction patterns. The TEM lamellas were prepared with FEI Strata DB 235 Focused Ion Beam (FIB), using the in-situ lift-out technique. The surface was coated with platinum to protect from ion damage during preparation, and a final polishing using 5 keV ions were used to minimize ion damage to the surface. Additionally, transmission Kikuchi diffraction (TKD) was performed in a Zeiss Merlin scanning electron microscope (SEM) on the lamella.

3. Results and discussion

3.1. Structure and element distribution in as-atomized powder

TEM was employed to characterize the microstructure, crystal structure and chemical distribution in the powder. Fig. 2 shows the TEM results from the as-atomized powder PSD 10–45 μm. The powder particles consist of several grains with a size of a few μm. A grain boundary within the powder particle is marked with a black arrow in the STEM image in Fig. 2. The grains exhibit different crystallographic orientations. Within each grain, a chemical fluctuation with Al/Ni rich regions and Cr/Fe rich regions are observed. The chemical composition of these regions can be seen in Table 1. This is identified as a dendritic growth, exhibiting a dendritic core (DC) and interdendritic regions (ID), as suggested by thermodynamic calculations in ref [15] where an Al/Ni rich B2 phase coexists with the liquid at high temperatures. An equimolar composition is expected when all liquid phase has solidified, as the alloy reaches equilibrium. Assuming that no equilibrium is reached during the gas atomization due to the high cooling rate, it is expected that the first solidifying phase is the Al/Ni rich B2 phase forming dendrites, while Cr and Fe is pushed out to the liquid and solidifies when the temperature is decreased further.

Table 1
Elemental composition of the dendritic core (DC) and interdendritic (ID) regions in at % determined with EDS.

Element	Al (at%)	Co (at%)	Cr (at%)	Fe (at%)	Ni (at%)
Dendritic core	20.2	21.1	17.9	19.3	21.5
Interdendritic region	13.3	21.2	22.9	21.6	21.0

The powder was further characterized by NBD in order to differentiate between the ordered B2 phase (primitive unit cell with space group $Pm\bar{3}m$) and the disordered bcc phase (body centred unit cell with space group $Im\bar{3}m$). NBD patterns were acquired from the DC and ID regions, respectively, within an individual grain. As can be seen in the diffraction patterns, the forbidden 100 reflection (indicated with a white circle) is present, indicating a primitive unit cell (this reflection is forbidden in the bcc structure). Furthermore, it is possible to enhance the contrast of two possible phases by dark field (DF) imaging in TEM mode. A DF image can be found in SI Fig. S2, where the entire analysed grain shows a similar contrast and therefore consists of a single crystalline structure but with an elemental variation as shown in Table 1. The error of the EDS measurements are within 1–2 at% due to the nature of the analysis, whereby only the separation of Al and Cr is significant.

Normalized diffraction patterns for the as-atomized condition with PSD 10–45 μm, from both neutron (ND) and synchrotron measurements (XRD) are shown in Fig. 3a. In agreement with the electron diffraction analysis in Fig. 2, all diffraction patterns can be indexed with a primitive cubic unit cell within the space group $Pm\bar{3}m$. No additional peaks or peak asymmetry were observed, suggesting a single-phase nature of the powder. For the neutron diffraction patterns, the 100 reflection is barely visible for the Cu-200 wavelength and non-visible for the Si-442 wavelength. This is

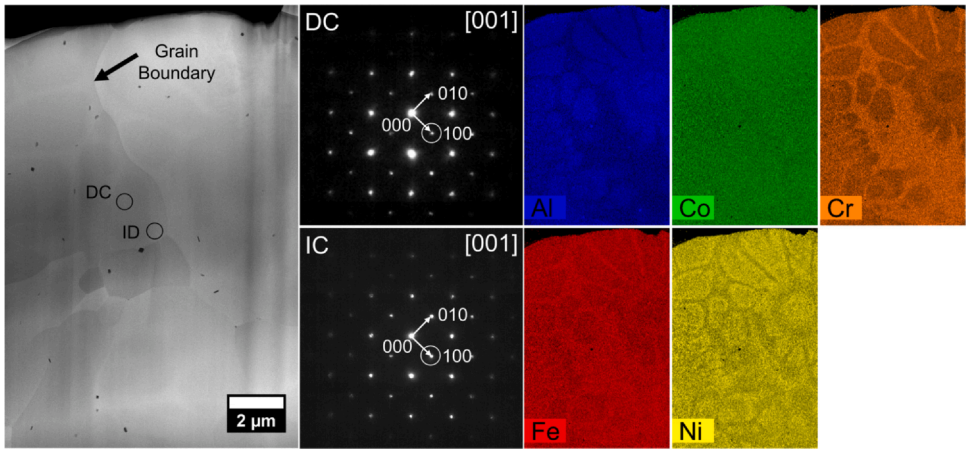

Fig. 2. STEM Z-contrast image of the as-atomized powder, showing nanobeam diffraction patterns in the [001] zone axis from the dendritic core (DC) and interdendritic (ID) regions in an individual grain. A grain boundary is marked with a black arrow in the STEM image, and the 100 reflection is marked with a white circle in the NBD patterns. The elemental distribution of Al, Co, Cr, Fe and Ni are shown in blue, green, orange, red and yellow, respectively.

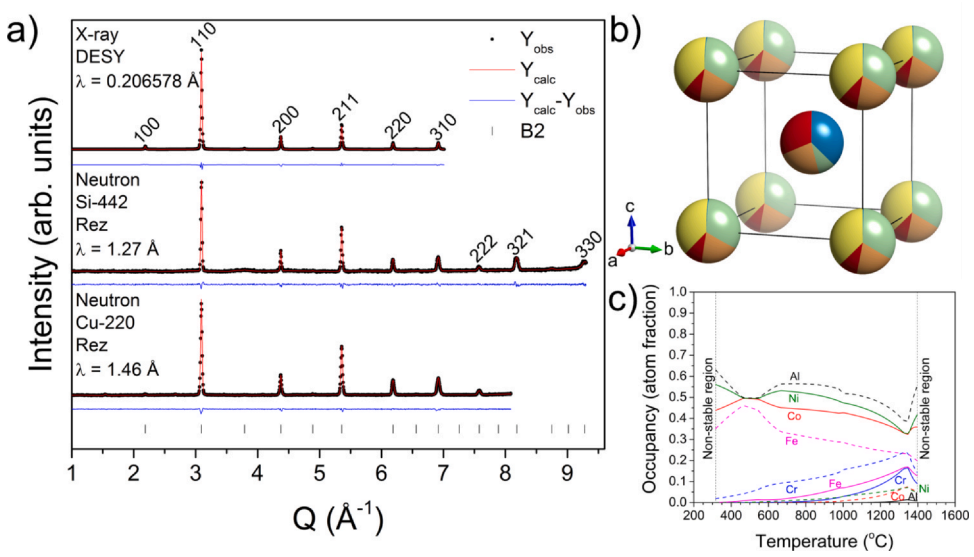

Fig. 3. a) Normalized powder diffraction patterns for NPD-Cu220, NPD-Si422 and synchrotron XRD. All diffraction patterns are refined using a single-phase B2 structure. b) refined occupancies in the B2-structure of the AlCoCrFeNi HEA. The elements Al, Co, Cr, Fe and Ni have the colours blue, green, orange, red and yellow, respectively. b) expected site occupancy for the B2 phase according to thermodynamic calculations of the two lattice positions (marked with solid and dashed lines), figure adapted from data from ref [15]. Figure adapted from data from ref [15].

likely due to the chemical occupancy of the two lattice positions, causing reduction of the intensity for the 100 reflection for neutrons in combination with a low flux of the neutron beam. Upon performing a combined refinement on the diffraction data from the two NPD patterns from MEREDIT and the XRD results from P02.1 at room temperature, all atomic occupancies could be refined. This refinement was possible due to the different scattering powers of the constituting elements of the HEA. The refinement confirmed the primitive cubic B2-phase in agreement with the predicted high-temperature phase [15]. The refined structure, Fig. 3b, shows the atomic occupation of the elements at the different lattice positions in the B2 structure. At the (0 0 0) position, the elements Co and Ni is dominating, whereas Al and Fe occupy mainly the (½ ½ ½) position. Lastly, Cr can be found to occupy both lattice positions without any indicated preference. Given that the enthalpy of formation for the binary compounds in the system are favourable to form bonds between both Fe and Al to Co and Ni, but not between Al and Fe, it is reasonable that Al and Fe occupying the same position in the B2 structure. This way the distance between Al and Fe is maximised. Cr has similar $\Delta H^{formation}$ to all elements, which is in line with the similar occupancy for both crystallographic sites [33]. Note that the refinement shows a summary of both DC and ID regions within the powder particles.

Fig. 2 illustrates the separation into two regions from TEM-EDS, DC and ID, with different chemical composition, whereas the powder diffraction patterns in Fig. 3 shows a single-phase character. This discrepancy can be explained by the fact that both regions observed in the TEM have the same crystal structure, B2, but with a small variation in chemical composition. The similar elemental distribution (Table 1) gives a very small difference of the unit cell parameters of the two regions, which makes them inseparable in powder diffraction techniques. The elemental segregation shown in Fig. 2 suggests that one B2 region forms with enhanced Al and Ni contents, while another B2 region forms with enhanced Fe and Cr contents. When combining the two almost identical regions into one powder diffraction resolved structure, it becomes comprehensible that Al and Fe occupies one crystallographic position, whereas the other position is richer in Co and Ni (Fig. 3b). The Cr is evenly distributed on the two positions in the crystal structure. This is in good agreement with the expected site occupation from thermodynamic calculations based on the CALPHAD method (Fig. 3c) originally published in ref. [15] but shown here for clarity of the discussion. The solid lines in Fig. 3c show the occupancy of the (0 0 0) position with high content of Ni and Co. In contrast, the dashed curves in Fig. 3c shows the occupancy at the (½ ½ ½) position with a clear predicted enrichment of Al and Fe at this position. It should be noted that Cr is evenly distributed between the two crystallographic positions, although a micrometre scale segregation can be seen (Fig. 2).

3.2. Structure and element distribution in annealed powder

As the CALPHAD calculations in Fig. 1 (adapted from ref. [15]) predict that the AlCoCrFeNi alloy has a complex phase composition at different temperatures, it is of interest to understand how annealing influences the phase composition of the powder. *In-situ* diffraction experiments were therefore performed for the PSD 10–45 µm during annealing up to 800–900 °C. The diffraction patterns from neutron and synchrotron radiations are shown in Fig. 4. For the neutron experiment, Fig. 4a, a low heating rate with a measuring time of 1 h was used for each step. The refinements of the obtained powder diffraction patterns show that a small amount of an fcc phase (space group $Fm\bar{3}m$) starts to form at low temperatures below 100 °C. The phase fraction of the fcc phase at 100 °C was, however, below 1%. The amount of fcc phase increases steadily up to 4.5% at 600 °C, where a σ phase (space group $P4/mmm$) starts to form. At 800 °C, the phase fractions are found to be 75%, 15% and 10% for the B2, fcc and σ phases, respectively. For the synchrotron XRD, a faster heating rate was used, 10 °C/min, and diffraction patterns were recorded continuously throughout the heating, seen in Fig. 4b. The trend of the evolution of phases is similar when comparing the two sets of in-situ experiments. However, the higher heating rate makes the phase transition occur at higher temperatures. The XRD patterns were recorded to 900 °C, and after 10 min at that temperature, similar phase fractions are observed as for the neutron experiment at 800 °C. Although the phase fractions in the two experiments are comparable at the end of the experiments, the secondary phases are much more evident with neutron scattering compared to X-rays. This is due to the differences in scattering lengths for the different elements for X-ray and neutron scattering, respectively, as well as that the compositions of the precipitates are not equiatomic. The fcc

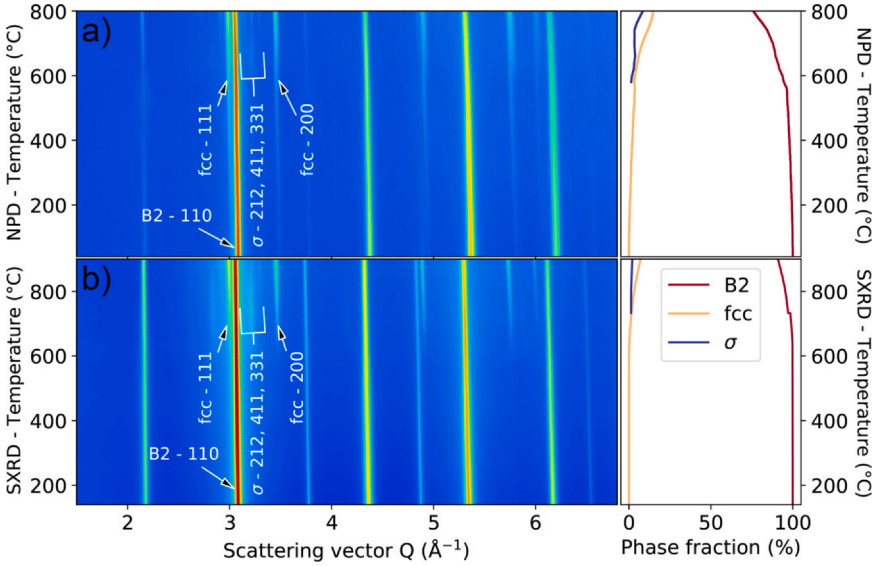

Fig. 4. a) In-situ neutron powder diffraction of the atomized powder with slow heating and long measurements for each temperature. b) In-situ synchrotron X-ray diffraction of the atomized powder with a heating rate of 10 °C/min and continuous measurements throughout the experiment. The refined phase fractions of the B2, fcc and σ phases are shown to the right of the diffraction patterns.

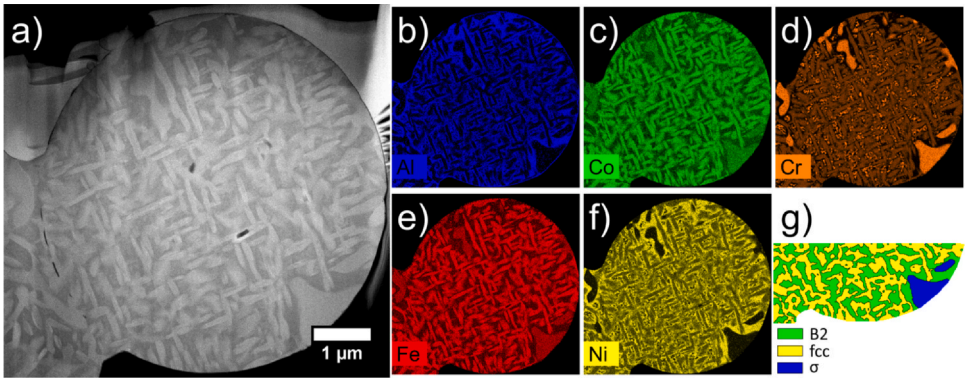

Fig. 5. a) STEM Z-contrast image of the powder (10–45 µm) after heat-treatment at 800 °C, b-f) elemental distribution and g) TKD showing the B2, fcc and σ phases as green, yellow and blue, respectively.

phase consists primarily of Co and Fe, whereas Cr is required to form the σ phase [15]. Furthermore, the primitive cubic peaks are clearly visible from the XRD, shown at ~2.1 and ~3.8 Å^{-1} in Fig. 5. This means that XRD is enough to observe the B2 structure but not to refine the atomic occupancies, given the almost identical X-ray scattering length for Co, Cr, Fe and Ni. Similar observations of the effect of different heat ratings have been shown in the AlCrFeMgNiSi HEA [23]. The decomposition of the B2 structure was heavily influenced by the moderate heating rate during conventional sintering or spark plasma sintering where very fast heating rates can be obtained.

The microstructure of the powder after annealing at 800 °C, using the same temperature profile as the neutron diffraction experiment, was studied with TEM (Fig. 5). The dendritic structure seen in Fig. 2 have vanished and instead a microstructure with brighter particles ordered in a lamellar-like fashion can be seen in a dark matrix. From EDS, it is evident that the brighter particles are enriched in Co, Cr and Fe while depleted in Al and Ni. The calculated equilibrium phases at 800 °C are B2 and σ [15]. Fig. 5g shows a phase map of a powder particle, where an fcc phase is observed to form in the B2 matrix, with some σ phase at the powder particle surface. The high amount of fcc phase compared to expectations from calculations in Fig. 1 could be explained by the relatively low formation kinetics for the σ phase, making it possible to form the fcc phase instead. The σ phase, with mainly Fe and Cr, forms primarily at the surface of the powder particles. Jepson et al. [34] showed preferred precipitation of a σ phase at the surface of duplex stainless steels and that the amount of σ phase formed depend on the quality of the surface. Furthermore, it has been described that the activation energy for the formation of the σ phase is closely related to the diffusion of Cr in the alloy, whereby initial formation at the surface could be explained by easier diffusion of Cr compared to inside the bulk alloy [35]. This is further understood by the sluggish formation of the σ phase in duplex stainless steels due to the large unit cell consisting of 32 atoms. The phase composition from TKD (not shown) is in good agreement with the refined composition from the neutron diffraction experiment, hence the results are representative of the powder.

Since the σ phase forms at the powder surface and a smaller powder particle results in a larger effective surface area, it should be expected that the size of the powder has an influence on the phase composition after annealing. Neutron diffraction was therefore carried out on the two PSDs, 10–45 µm and < 32 µm, after annealing up to 800 °C and cooling to room temperature. The results (see SI Fig. S3 for the diffractograms) show, as expected, a decomposition of the B2 phase for both fractions into the same decomposition products (B2, fcc and σ phases). However, as can be seen in Table 2, the phase composition of the two PSDs are different, with significantly more σ phase in the PSD < 32 µm. As the effective surface area is larger for the smaller grains, diffusion is easily activated and Cr atoms can

Table 2
Refined phase fractions in wt% for the sieving fractions 10–45 µm and < 32 µm at RT after in-situ annealing.

Phase	10–45 µm	< 32 µm
B2 (wt%)	73.6(7)	56.0(6)
fcc (wt%)	12.0(1)	12.6(1)
σ (wt%)	14.4(5)	31.4(2)

Table 3
Phase fractions in wt% for the sintered samples from as-atomized and pre-annealed powder obtained from Rietveld refinements of XRD data.

Phase	As-atomized	Pre-annealed
B2 (wt%)	44(2)	50(1)
fcc (wt%)	26.0(5)	33.7(4)
σ (wt%)	29.5(7)	16.7(2)

move to form the σ phase at the powder particle surface, as shown in Fig. 5.

3.3. Pre-annealing of powder as a design route in sintering of AlCoCrFeNi parts

The results above clearly show that the phase composition of a powder is influenced by a pre-annealing step and PSD. Therefore, it is interesting to investigate if the phase composition of the powder affects the final phase composition and microstructure of sintered components. Fig. 6a shows XRD patterns and corresponding Rietveld refinements for the samples produced from as-atomized and annealed powder with a grain size of < 32 µm. All peaks in the diffraction patterns can be indexed by a combination of σ, fcc and B2 phases, but with varying intensities between the different samples. The phase composition of the samples (estimated by Rietveld refinements) are summarized in Table 3. It is clear that the sample from the sintered as-atomized powder has a significantly higher amount of σ phase and less B2 and fcc. In this experiment, a sintering cycle with target temperature of 1320 °C and a holding time of 4 h was used. This was followed by a slower furnace cooling (no quenching). Based on the CALPHAD results in Fig. 1 and binder jetting studies in ref. [15], it is expected that the pure B2 phase is formed at the sintering temperature and that fcc and σ phase is reformed during the cooling step in the furnace.

Fig. 6b and c show the microstructures of the samples produced from as-atomized and pre-annealed powder, respectively. A microstructure that is similar to AlCoCrFeNi produced by binder jetting [15] is obtained after sintering of the as-atomized powder. An illustration of how the phases are ordered in the material can be seen in the inset, showing the distribution of secondary phases forming within the B2 grains and at the grain boundaries. The phase forming inside the grains is mainly the σ phase, while an fcc phase forms at the grain boundaries. For the sample produced from the pre-annealed powder, however, the microstructure is very different (Fig. 6c). Large grains, attributed to the fcc phase, are shown in Fig. 6b to be well distributed in the sintered sample. The B2 grains are not as well defined as for the sample produced from the as-atomized powder, as an interconnecting network of the B2/fcc phases has formed instead. The amount of σ phase within the B2 grains has also decreased significantly, in good agreement with the estimation from the XRD patterns.

A possible explanation for the difference between the two powders is that the annealed powder has an enrichment of Fe and Cr in the σ phase formed at the surface. Hence, the interior of the starting powder grains is depleted with Fe and Cr. In contrast, the as-atomized powder still has high concentrations of Fe and Cr in the bulk of the grains. During sintering at 1320 °C, the alloy will start to transform into the stable B2 structure, in agreement with thermodynamics. Upon cooling, there will be a driving force to form σ phase, but this requires the presence of high concentrations of Fe and Cr. For the as-atomized powder condition, which still has significant amounts of these elements inside the interior of the particles, the σ phase will therefore precipitate inside the B2 grain, as shown in Fig. 6c. Below 600 °C, the σ phase will decompose, but this requires a significant solid-state diffusion. If the diffusion is too slow, large amounts of σ phase will remain inside the B2 grains. In the pre-annealed powder condition the Fe and Cr are enriched at the surface, forming σ phase in grain boundaries of the sintered sample during heating. The diffusion rate is much higher at the grain boundaries, leading to faster decomposition of the σ phase upon cooling. In comparison, the lower concentration of Fe and Cr inside the pre-annealed powder particles implies formation of fewer σ phase precipitates in the B2 grain interior as shown in Fig. 6c. It should be noted, however, that the formation of the fcc phase in Fig. 6b and c also can be affected by the remaining binder. The binder contains

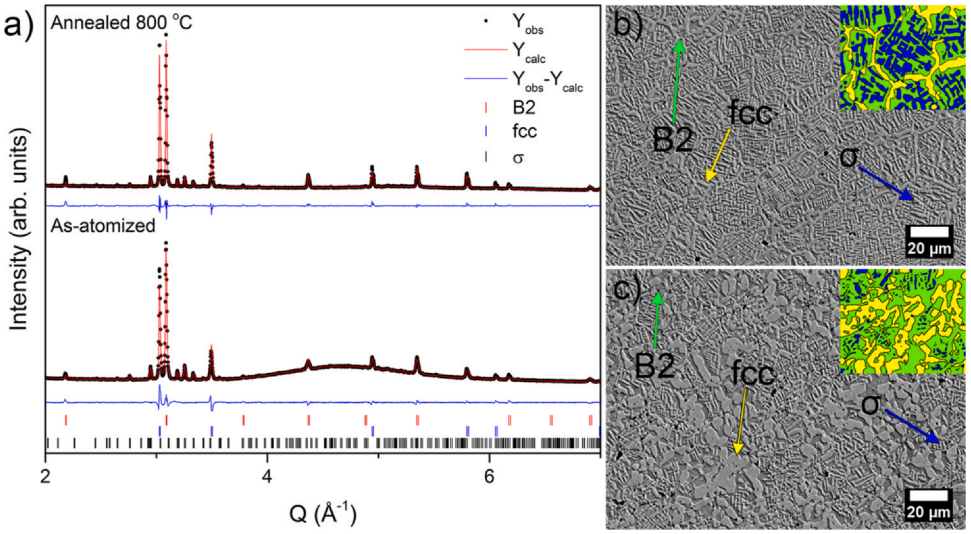

Fig. 6. a) XRD patterns of samples sintered from as-atomized and annealed powder. b) and c) show the microstructures by secondary electron SEM images of the samples produced from as-atomized and annealed powder, respectively. The insets in b) and c) illustrates the microstructure with the B2, fcc and σ phases marked with green, yellow and blue colours.

carbon, which upon heating carbon can diffuse into the microstructure and stabilize the fcc phase as carbon is a common austenitic former in stainless steels.

The results indicate that the resulting microstructure after sintering can be designed by pre-annealing of the powder, reducing the amount of the brittle σ phase by careful design of the annealing temperature. This would be beneficial for the mechanical properties, as the σ phase is commonly known to decrease toughness in, e.g. duplex stainless steels and is avoided by quenching from high temperatures after a solution treatment [36]. The samples presented here contain some porosity, but optimization of the density was outside the scope of this study.

4. Conclusions

In this study, the effects of thermal treatments on the HEA AlCoCrFeNi powder alloy produced via inert gas atomization have been studied. It has been shown from a combination of electron, synchrotron X-ray and neutron diffraction that the as-atomized compound crystallises in an ordered B2 phase with a preference of Al and Fe on the (½ ½ ½) site while Co and Ni preferably occupy the (0 0 0) position. *In-situ* diffraction also reveals that the B2 phase decomposes at higher temperatures into fcc and σ phases. The thermal onset of the phase transformations is, however, dependent on the heating rate, where a lower heating rate results in a decreased onset temperature for the phase transformation. The conversion of the B2 phase has been confirmed by TEM analysis after the heat-treatments of the powders. In addition, the size of the particles from the atomization is important for the decomposition behaviour. The diffusion of Cr is higher at the particle surfaces, giving rise to a larger amount of σ phase forming for the smaller particle size distribution with a larger effective surface area. Finally, it was demonstrated that the pre-annealing of the atomized powder influences the microstructure of sintered parts, with a lower amount of σ phase in the final component if a pre-annealing step of the powder is employed. Hence, it can be concluded that the microstructure can be designed by proper selection of the feedstock material used for manufacturing.

CRediT authorship contribution statement

DK planned the study with UJ and JC. DK synthesized the samples. DK, PH, UJ, and JC wrote the paper, all authors read, contributed and commented on the manuscript. DK, JCT, PB and JC performed X-ray and neutron characterization and structural refinements. DK and LR performed microscopy analysis.

Declaration of Competing Interest

The authors declare that they have no known competing financial interests or personal relationships that could have appeared to influence the work reported in this paper.

Acknowledgement

Financial support from the Swedish Foundation for Strategic Research, project “SSF – Development of processes and Materials in AM”, Reference No. GMT14–0048, is greatly acknowledged. JC acknowledges the Swedish Research Council (VR) for financial support. We acknowledge DESY (Hamburg, Germany), a member of the Helmholtz Association HGF, for the provision of experimental facilities (beamline P02.1). Measurements were carried out at the CANAM infrastructure of the NPI CAS Rez supported through MEYS project No. LM2015056. Also, the support from Thomas Hansen during the beam time at ILL is acknowledged.

Appendix A. Supporting information

Supplementary data associated with this article can be found in the online version at doi:10.1016/j.jallcom.2021.162060.

References

[1] B. Cantor, I.T.H. Chang, P. Knight, A.J.B. Vincent, Microstructural development in equiatomic multicomponent alloys, Mat. Sci. Eng. a-Struct. 375 (2004) 213–218, https://doi.org/10.1016/j.msea.2003.10.257
[2] J.W. Yeh, et al., Nanostructured high-entropy alloys with multiple principal elements: novel alloy design concepts and outcomes, Adv. Eng. Mater. 6 (5) (2004) 299–303, https://doi.org/10.1002/adem.200300567
[3] O.N. Senkov, G.B. Wilks, J.M. Scott, D.B. Miracle, Mechanical properties of Nb25Mo25Ta25W25 and V20Nb20Mo20Ta20W20 refractory high entropy alloys, Intermetallics 19 (5) (2011) 698–706, https://doi.org/10.1016/j.intermet.2011.01.004
[4] B. Gludovatz, A. Hohenwarter, D. Catoor, E.H. Chang, E.P. George, R.O. Ritchie, A fracture-resistant high-entropy alloy for cryogenic applications, Science 345 (6201) (2014) 1153–1158, https://doi.org/10.1126/science.1254581
[5] Z. Li, K.G. Pradeep, Y. Deng, D. Raabe, C.C. Tasan, Metastable high-entropy dual-phase alloys overcome the strength-ductility trade-off, Nature 534 (7606) (2016) 227–230, https://doi.org/10.1038/nature17981
[6] Z.M. Li, C.C. Tasan, K.G. Pradeep, D. Raabe, A TRIP-assisted dual-phase high-entropy alloy: grain size and phase fraction effects on deformation behavior (in English), Acta Mater. 131 (2017) 323–335, https://doi.org/10.1016/j.actamat.2017.03.069
[7] M.H. Chuang, M.H. Tsai, W.R. Wang, S.J. Lin, J.W. Yeh, Microstructure and wear behavior of AlxCo1.5CrFeNi1.5Tiy high-entropy alloys, Acta Mater. 59 (16) (2011) 6308–6317, https://doi.org/10.1016/j.actamat.2011.06.041
[8] M.H. Chuang, M.H. Tsai, C.W. Tsai, N.H. Yang, S.Y. Chang, J.W. Yeh, S.K. Chen, S.J. Lin, Intrinsic surface hardening and precipitation kinetics of Al0.3CrFe1.5MnNi0.5 multi-component alloy, J. Alloy. Compd. 551 (2013) 12–18, https://doi.org/10.1016/j.jallcom.2012.09.133
[9] G. Laplanche, U.F. Volkert, G. Eggeler, E.P. George, Oxidation behavior of the CrMnFeCoNi high-entropy alloy, Oxid. Met 85 (5–6) (2016) 629–645, https://doi.org/10.1007/s11085-016-9616-1
[10] T.M. Butler, M.L. Weaver, Oxidation behavior of arc melted AlCoCrFeNi multi-component high-entropy alloys, J. Alloy. Compd. 674 (2016) 229–244, https://doi.org/10.1016/j.jallcom.2016.02.257
[11] T. Fujieda, H. Shiratori, K. Kuwabara, M. Hirota, T. Kato, K. Yamanaka, Y. Koizumi, A. Chiba, S. Watanabe, CoCrFeNiTi-based high-entropy alloy with superior tensile strength and corrosion resistance achieved by a combination of additive manufacturing using selective electron beam melting and solution treatment, Mater. Lett. 189 (2017) 148–151, https://doi.org/10.1016/j.matlet.2016.11.026
[12] M. Sahlberg, D. Karlsson, C. Zlotea, U. Jansson, Superior hydrogen storage in high entropy alloys, Sci. Rep. 6 (2016) 36770, https://doi.org/10.1038/srep36770
[13] D. Karlsson, G. Ek, J. Cedervall, C. Zlotea, K.T. Møller, T.C. Hansen, J. Bednarčík, M. Paskevicius, M.H. Sørby, T.R. Jensen, U. Jansson, M. Sahlberg, Structure and hydrogenation properties of a HfNbTiVZr high-entropy alloy, Inorg. Chem. 57 (4) (2018) 2103–2110, https://doi.org/10.1021/acs.inorgchem.7b03004
[14] D.B. Miracle, O.N. Senkov, A critical review of high entropy alloys and related concepts, Acta Mater. 122 (2017) 448–511, https://doi.org/10.1016/j.actamat.2016.08.081
[15] D. Karlsson, G. Lindwall, A. Lundbäck, M. Amnebrink, M. Boström, L. Riekehr, M. Schuisky, M. Sahlberg, U. Jansson, Binder jetting of the AlCoCrFeNi alloy, Addit. Manuf. 27 (2019) 72–79, https://doi.org/10.1016/j.addma.2019.02.010
[16] T.M. Butler, M.L. Weaver, Investigation of the phase stabilities in AlNiCoCrFe high entropy alloys, J. Alloy. Compd. 691 (2017) 119–129, https://doi.org/10.1016/j.jallcom.2016.08.121
[17] W.R. Wang, W.L. Wang, S.C. Wang, Y.C. Tsai, C.H. Lai, J.W. Yeh, Effects of Al addition on the microstructure and mechanical property of AlxCoCrFeNi high-entropy alloys, Intermetallics 26 (2012) 44–51, https://doi.org/10.1016/j.intermet.2012.03.005
[18] W.-R. Wang, W.-L. Wang, J.-W. Yeh, Phases, microstructure and mechanical properties of AlxCoCrFeNi high-entropy alloys at elevated temperatures, J. Alloy. Compd. 589 (2014) 143–152, https://doi.org/10.1016/j.jallcom.2013.11.084
[19] A. Manzoni, H. Daoud, R. Volkl, U. Glatzel, N. Wanderka, Phase separation in equiatomic AlCoCrFeNi high-entropy alloy, Ultramicroscopy 132 (2013) 212–215, https://doi.org/10.1016/j.ultramic.2012.12.015
[20] D. Karlsson, A. Marshal, F. Johansson, M. Schuisky, M. Sahlberg, J.M. Schneider, U. Jansson, Elemental segregation in an AlCoCrFeNi high-entropy alloy - a comparison between selective laser melting and induction melting, J. Alloy. Compd. 784 (2018) 195–203, https://doi.org/10.1016/j.jallcom.2018.12.267
[21] V. Shivam, J. Basu, V.K. Pandey, Y. Shadangi, N.K. Mukhopadhyay, Alloying behaviour, thermal stability and phase evolution in quinary AlCoCrFeNi high entropy alloy, Adv. Powder Technol. 29 (9) (2018) 2221–2230, https://doi.org/10.1016/j.apt.2018.06.006
[22] V. Shivam, J. Basu, Y. Shadangi, M.K. Singh, N.K. Mukhopadhyay, Mechano-chemical synthesis, thermal stability and phase evolution in AlCoCrFeNiMn high entropy alloy, J. Alloy. Compd. 757 (2018) 87–97, https://doi.org/10.1016/j.jallcom.2018.05.057
[23] N. Singh, Y. Shadangi, V. Shivam, N.K. Mukhopadhyay, MgAlSiCrFeNi low-density high entropy alloy processed by mechanical alloying and spark plasma sintering:

Effect on phase evolution and thermal stability, J. Alloy. Compd. vol. 875, (2021) 159923, https://doi.org/10.1016/j.jallcom.2021.159923
[24] T. Fujieda, H. Shiratori, K. Kuwabara, T. Kato, K. Yamanaka, Y. Koizumi, A. Chiba, First demonstration of promising selective electron beam melting method for utilizing high-entropy alloys as engineering materials, Mater. Lett. 159 (2015) 12–15, https://doi.org/10.1016/j.matlet.2015.06.046
[25] H. Shiratori, T. Fujieda, K. Yamanaka, Y. Koizumi, K. Kuwabara, T. Kato, A. Chiba, Relationship between the microstructure and mechanical properties of an equiatomic AlCoCrFeNi high-entropy alloy fabricated by selective electron beam melting, Mat. Sci. Eng. a-Struct. vol. 656, (2016) 39–46, https://doi.org/10.1016/j.msea.2016.01.019
[26] F. Pengjun, X. Yi, L. Xinggang, C. Ya, Influence of atomizing gas and cooling rate on solidification characterization of nickel-based superalloy powders, Rare Met. Mater. Eng. 47 (2) (2018) 423–430, https://doi.org/10.1016/s1875-5372(18)30082-1
[27] M.J. Carrington, J. Daure, V.L. Ratia, P.H. Shipway, D.G. McCartney, D.A. Stewart, Microstructural characterisation of Tristelle 5183 (Fe-21%Cr-10%Ni-7.5%Nb-5%Si-2%C in wt%) alloy powder produced by gas atomisation, Mater. Des. 164 (2019) 107548, https://doi.org/10.1016/j.matdes.2018.107548
[28] B.L. Zheng, Y.J. Lin, Y.Z. Zhou, E.J. Lavernia, Gas atomization of amorphous aluminum powder: Part II. Experimental investigation, Met. Mater. Trans. B 40 (6) (2009) 995–1004, https://doi.org/10.1007/s11663-009-9277-4
[29] T.R. Jensen, T.K. Nielsen, Y. Filinchuk, J.E. Jørgensen, Y. Cerenius, E.M. Gray, C.J. Webb, Versatile in situ powder X-ray diffraction cells for solid-gas investigations, J. Appl. Crystallogr 43 (Pt 6) (2010) 1456–1463, https://doi.org/10.1107/S0021889810038148
[30] H.M. Rietveld, A profile refinement method for nuclear and magnetic structures, J. Appl. Crystallogr. 2 (2) (1969) 65–66, https://doi.org/10.1107/S0021889869006558
[31] J. Rodríguez-Carvajal, Recent advances in magnetic structure determination by neutron powder diffraction, Phys. B: Condens. Matter 192 (1–2) (1993) 55–69, https://doi.org/10.1016/0921-4526(93)90108-i
[32] A.P. Hammersley, S.O. Svensson, M. Hanfland, A.N. Fitch, D. Hausermann, Two-dimensional detector software: From real detector to idealised image or two-theta scan, High. Press. Res. 14 (4–6) (1996) 235–248, https://doi.org/10.1080/08957959608201408
[33] M.C. Troparevsky, J.R. Morris, P.R.C. Kent, A.R. Lupini, G.M. Stocks, Criteria for predicting the formation of single-phase high-entropy alloys, Phys. Rev. X 5 (1) (2015) 011041, https://doi.org/10.1103/PhysRevX.5.011041
[34] M.A.E. Jepson, M. Rowlett, R.L. Higginson, The effect of surface preparation on the precipitation of sigma during high temperature exposure of S32205 duplex stainless steel, Metall. Mater. Trans. A 48 (3) (2017) 1491–1500, https://doi.org/10.1007/s11661-016-3914-8
[35] R. Magnabosco, Kinetics of sigma phase formation in a duplex stainless steel, Mater. Res-Ibero-Am. J. 12 (3) (2009) 321–327, https://doi.org/10.1590/S1516-14392009000300012
[36] S. Atamert, J.E. King, Sigma-phase formation and its prevention in duplex stainless steels, J. Mater. Sci. Lett. 12 (14) (1993) 1144–1147, https://doi.org/10.1007/bf00420548